The Astrophysical Journal, 977:112 (16pp), 2024 December 10 https://doi.org/10.3847/1538-4357/ad8dcd

A Census of Dwarf Galaxy Satellites around LMC-mass Galaxy NGC 2403*

Jeffrey L. Carlin[1], David J. Sand[2], Burçin Mutlu-Pakdil[3], Denija Crnojević[4], Amandine Doliva-Dolinsky[4,5], Christopher T. Garling[6], Annika H. G. Peter[7], Jean P. Brodie[8,9], Duncan A. Forbes[10], Jonathan R. Hargis[11], Aaron J. Romanowsky[12,13], Kristine Spekkens[14], Jay Strader[15], and Beth Willman[16]
[1] AURA/Rubin Observatory, 950 North Cherry Avenue, Tucson, AZ 85719, USA; jcarlin@lsst.org, jeffreylcarlin@gmail.com
[2] Department of Astronomy/Steward Observatory, 933 North Cherry Avenue, Rm. N204, Tucson, AZ 85721-0065, USA
[3] Department of Physics and Astronomy, Dartmouth College, Hanover, NH 03755, USA
[4] Department of Physics & Astronomy, University of Tampa, 401 West Kennedy Boulevard, Tampa, FL 33606, USA
[5] Department of Physics & Astronomy, Dartmouth College, Hanover, NH 03755, USA
[6] Department of Astronomy, University of Virginia, 530 McCormick Road, Charlottesville, VA 22904, USA
[7] CCAPP, Department of Physics, and Department of Astronomy, The Ohio State University, Columbus, OH 43210, USA
[8] Centre for Astrophysics and Supercomputing, Swinburne University, John Street, Hawthorn VIC 3122, Australia
[9] Department of Astronomy & Astrophysics, University of California Santa Cruz, 1156 High Street, Santa Cruz, CA 95064, USA
[10] Centre for Astrophysics and Supercomputing, Swinburne University, Hawthorn VIC 3122, Australia
[11] Space Telescope Science Institute, 3700 San Martin Drive, Baltimore, MD 21218, USA
[12] University of California Observatories, 1156 High Street, Santa Cruz, CA 95064, USA
[13] Department of Physics & Astronomy, San José State University, One Washington Square, San Jose, CA 95192, USA
[14] Department of Physics, Engineering Physics, and Astronomy, Queen's University, Kingston, ON, K7L 3N6, Canada
[15] Center for Data Intensive and Time Domain Astronomy, Department of Physics and Astronomy, Michigan State University, East Lansing, MI 48824, USA
[16] LSST Discovery Alliance, 933 North Cherry Avenue, Tucson, AZ 85719, USA
Received 2024 September 6; revised 2024 October 23; accepted 2024 October 25; published 2024 December 6

Abstract

We present the first comprehensive census of the satellite population around a Large Magellanic Cloud stellar-mass galaxy, as part of the Magellanic Analog Dwarf Companions and Stellar Halos (MADCASH) survey. We have surveyed NGC 2403 ($D = 3.0$ Mpc) with the Subaru/Hyper Suprime-Cam imager out to a projected radius of 90 kpc (with partial coverage extending out to ∼110 kpc, or ∼80% of the virial radius of NGC 2403), resolving stars in the uppermost ∼2.5 mag of its red giant branch. By looking for stellar overdensities in the red giant branch spatial density map, we identify 149 satellite candidates, of which only the previously discovered MADCASH J074238+65201-dw is a bona fide dwarf, together with the more massive and disrupting satellite DDO 44. We carefully assess the completeness of our search via injection of artificial dwarf galaxies into the images, finding that we are reliably sensitive to candidates down to $M_V \sim -7.5$ mag (and somewhat sensitive to even fainter satellites). A comparison of the satellite luminosity function of NGC 2403 down to this magnitude limit to theoretical expectations shows overall good agreement. This is the first of a full sample of 11 Magellanic Cloud–mass host galaxies we will analyze, creating a statistical sample that will provide the first quantitative constraints on hierarchical models of galaxy formation around low-mass hosts.

Unified Astronomy Thesaurus concepts: Dwarf galaxies (416); Galaxy stellar halos (598); Dwarf spheroidal galaxies (420); Tidal disruption (1696); Galaxy interactions (600); Stellar photometry (1620); Magellanic Clouds (990); Galaxy dark matter halos (1880)

1. Introduction

The lowest-mass galaxies are powerful tools for understanding galaxy evolution, dark matter, and cosmology (e.g., J. S. Bullock & M. Boylan-Kolchin 2017; J. D. Simon 2019; L. V. Sales et al. 2022). In particular, the faint end of the galaxy luminosity function (LF) can probe how baryons populate the smallest dark matter halos, including how they are affected by various astrophysical processes such as reionization (e.g., J. S. Bullock et al. 2000; M. Ricotti & N. Y. Gnedin 2005; E. Applebaum et al. 2021), supernova/star formation feedback (e.g., M.-M. Mac Low & A. Ferrara 1999; K. El-Badry et al. 2018), and tidal/ram-pressure stripping (e.g., A. Gatto et al. 2013; C. M. Simpson et al. 2018).

Ultrafaint dwarf galaxies continue to be found around the Milky Way (e.g., S. E. T. Smith et al. 2023; W. Cerny et al. 2023) and at the edge of the Local Group (e.g., D. J. Sand et al. 2022; M. G. Jones et al. 2023; K. B. W. McQuinn et al. 2023; K. B. W. McQuinn et al. 2024), which will remain a vital proving ground for galaxy formation and dark matter models (e.g., E. O. Nadler et al. 2024). Beyond the Local Group, faint and ultrafaint dwarf galaxy populations are being identified around Milky Way–mass systems using resolved-star searches (K. Chiboucas et al. 2013; D. Crnojević et al. 2016; A. Smercina et al. 2018; D. Crnojević et al. 2019; P. Bennet et al. 2019, 2020; B. Mutlu-Pakdil et al. 2024), diffuse galaxy identification (P. Bennet et al. 2017; A. B. Davis et al. 2021; S. G. Carlsten et al. 2022; D. Zaritsky et al. 2024), and spectroscopic surveys (M. Geha et al. 2017; Y.-Y. Mao et al. 2021, 2024). These programs, largely conducted on Milky Way–mass galaxies, are elucidating the typical number and scatter in satellite properties as a function of mass, environment, and accretion history (e.g., P. Bennet et al. 2019; S. G. Carlsten et al. 2022; A. Smercina et al. 2022; M. Geha et al. 2024; B. Mutlu-Pakdil et al. 2024).

* This research is based on data collected at the Subaru Telescope, which is operated by the National Astronomical Observatory of Japan.

Table 1
Properties of NGC 2403

Parameter	Value	References
R.A. (J2000)	$07^{h}36^{m}51\overset{s}{.}4$	NASA/IPAC Extragalactic Database (NED)
Decl. (J2000)	$+65°36'09\overset{''}{.}2$	NED
Distance (Mpc)	3.0	J. L. Carlin et al. (2016)
Virial Radius (kpc)[a]	140	B. Mutlu-Pakdil et al. (2021)
Stellar Mass ($M_{\odot}$)	7.2×10^{9}	G. A. Dooley et al. (2017)
Halo Mass ($M_{\odot}$)[b]	3.4×10^{11}	B. Mutlu-Pakdil et al. (2021)

Notes.
[a] Calculated using the definition from G. L. Bryan & M. L. Norman (1998).
[b] Inferred using the stellar mass–halo mass relation from B. P. Moster et al. (2010).

To complement these studies at the Milky Way–mass scale, we must also measure the low–mass galaxy population in a variety of environments, from the field- to galaxy-cluster scale. An intriguing avenue is the dwarf satellite population of relatively massive dwarf galaxy systems at the Magellanic Cloud (MC)–mass scale, which are expected in cold dark matter models (e.g., G. A. Dooley et al. 2017; I. M. E. Santos-Santos et al. 2022). At this mass scale, tidal and ram-pressure stripping should be weakened, allowing for a deeper understanding of these processes and how they affect the smallest galaxies. The ultrafaint satellite population of the Large Magellanic Cloud (LMC) itself is now coming into focus, thanks to Gaia orbital information (e.g., N. Kallivayalil et al. 2018; G. Battaglia et al. 2022). Beyond the Local Group, initial studies have yielded promising results (e.g., D. J. Sand et al. 2015; J. L. Carlin et al. 2016; C. T. Garling et al. 2021; D. J. Sand et al. 2024), but quantitative satellite LFs are largely still lacking at this mass scale.

Here we present a quantitative satellite LF for the nearby galaxy NGC 2403. NGC 2403 is an AB-type spiral galaxy and a stellar mass analog of the LMC ($D = 3.0$ Mpc; $M_{*} \sim 7 \times 10^{9}\ M_{\odot}$, or $2\times$ the stellar mass of the LMC; a summary of NGC 2403 properties adopted in this work is in Table 1). This galaxy is part of the ongoing Magellanic Analog Dwarf Companions and Stellar Halos (MADCASH) survey (see Section 2); previous results from the survey include the initial discovery of MADCASH-1 (MADCASH J074238+652501-dw; J. L. Carlin et al. 2016), a faint satellite galaxy ($M_V = -7.8$ mag) of NGC 2403 with an old and metal-poor stellar population and no apparent H I gas reservoir. Follow-up imaging with the Hubble Space Telescope confirmed that MADCASH-1 contains solely ancient, metal-poor stars and is at a distance consistent with being an NGC 2403 satellite (J. L. Carlin et al. 2021). The full red giant branch (RGB) halo map of NGC 2403 revealed a tidal stream associated with the previously known massive satellite DDO 44 ($M_V = -12.9$ mag; J. L. Carlin et al. 2019). The data presented here have also contributed to a study of the old star clusters in NGC 2403 and their age–metallicity relation (D. A. Forbes et al. 2022). In Section 2, we briefly describe the MADCASH survey and its goal of probing substructure in MC analog systems. In Section 3, we describe the deep Subaru Hyper Suprime-Cam (HSC) data of NGC 2403's halo, data reduction, and the dwarf galaxy search. In Section 4, we discuss our injection of artificial dwarf galaxies into the image-level data to quantitatively derive our completeness limits. Finally, in Section 5, we present the satellite LF of NGC 2403, placing its dwarf galaxy system in context and comparing it with expectations from cosmological simulations.

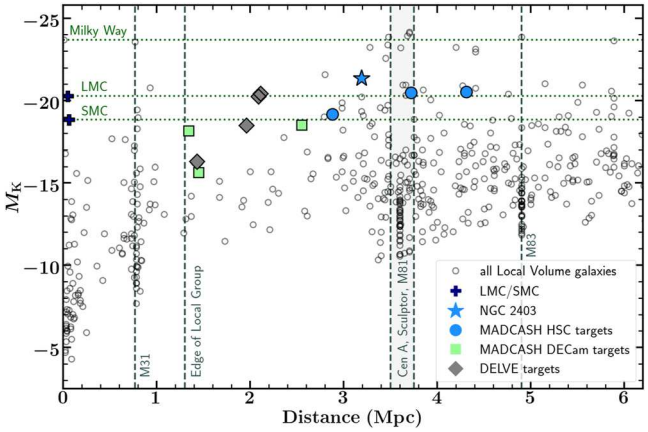

Figure 1. Absolute K-band luminosity (M_K) vs. distance for Local Volume galaxies from the catalog of I. D. Karachentsev et al. (2013). MC analog host galaxies (i.e., galaxies with stellar masses $\frac{1}{3}M_{*,\,\mathrm{SMC}} < M_{*} < 3M_{*,\,\mathrm{LMC}}$) targeted by the MADCASH and DELVE-DEEP surveys are highlighted, with the subject of this work (NGC 2403) shown as a blue star.

2. The MADCASH Survey

In order to probe the satellite population of nearby LMC-mass galaxies, we have undertaken the MADCASH survey. MADCASH is an observational effort to obtain deep, resolved-star maps of the halos of isolated MC-mass galaxies. To efficiently map large areas to depths at least 1–2 mag below the RGB tip (TRGB) in nearby ($D \lesssim 4$ Mpc) MC analogs requires large field-of-view imagers on large-aperture telescopes. For MADCASH, we have used the Dark Energy Camera (DECam) on the Blanco 4 m at CTIO and HSC on the Subaru 8.2 m in Hawaii. Figure 1 shows the absolute K-band luminosity versus distance for all galaxies from the Local Volume catalog of I. D. Karachentsev et al. (2013)[17] as small open circles, with colored, filled points representing objects targeted in our MADCASH survey (green squares and blue circles) and a sister program with DECam, the DELVE-DEEP survey (A. Drlica-Wagner et al. 2021; gray filled diamonds). The eleven highlighted points are the only targets with stellar masses within a factor of 3 of either the SMC or LMC, at distances where their individual RGB stars can be resolved and accessible with either HSC or DECam.[18] The combined HSC and DECam data sets will map nearly the entire virial volumes of these 11 hosts. The properties of the systems we have observed with Subaru+HSC are given in Table 2; DECam results will be presented in a separate work. In this particular paper, we provide a systematic look at the results from a deep survey of the halo of NGC 2403 with HSC; a comprehensive census of satellites in all four systems from Table 2 will appear in future work.

[17] Available at https://www.sao.ru/lv/lvgdb/.
[18] While one can see in Figure 1 that there are more than 11 galaxies in the stellar mass and distance range of our sample selection, many of them do not make it into the final sample for a variety of reasons. Many are at declinations too far north to be observed with Subaru. In the southern sky, we limit the host sample to those within $D \lesssim 2.5$ Mpc; more distant systems would require prohibitive exposure times with the 4 m Blanco Telescope. A few objects were removed because of high extinction along their line of sight, and one (NGC 404) was culled from the sample because it has a second-magnitude star only a few arcminutes away.

Table 2
Properties of the MADCASH Host Galaxies Being Observed with Subaru +HSC, plus the SMC and LMC for Context

Galaxy	M_{stars}[a] ($M_\odot$)	D[a] (Mpc)	R_{vir}[a] (kpc)	$N_{sat,exp}$[b]
***SMC	7.0×10^8	0.06	⋯	1–3
NGC 4214	1.0×10^9	2.9	100	1–5
***LMC	2.6×10^9	0.05	⋯	2–5
NGC 247	3.2×10^9	3.7	120	2–6
NGC 4244	3.5×10^9	4.3	120	2–6
NGC 2403	7.2×10^9	3.0	140	4–8

Notes.
[a] Stellar masses, distances, and virial radii are from B. Mutlu-Pakdil et al. (2021), except the distance to NGC 2403, which is from J. L. Carlin et al. (2016).
[b] Predicted number of satellites with $M_{stars} > 10^5\ M_\odot$ from (G. A. Dooley et al. 2017), based on the S. Garrison-Kimmel et al. (2017) models. The range represents the 20th–80th percentile range of predictions for each host.

3. Data and Analysis

We observed seven pointings around NGC 2403 with HSC (H. Furusawa et al. 2018; S. Kawanomoto et al. 2018; Y. Komiyama et al. 2018; S. Miyazaki et al. 2018) on the Subaru 8.2 m telescope at Maunakea (Hawaii); see Figure 2 for a depiction of our data's photometric depth as a function of position. The 1.°5 diameter HSC field of view, corresponding to a projected diameter of ∼80 kpc at the distance of NGC 2403, enabled us to efficiently survey the surroundings of NGC 2403 out to large projected distances. The seven HSC pointings we obtained cover the entire area out to a projected radius of 90 kpc from the center of NGC 2403 (assuming $D = 3.01$ Mpc as measured by J. L. Carlin et al. 2016) and ∼60% of the area between 90 and 110 kpc in projected distance. The estimated virial radius of NGC 2403 is ∼140 kpc (B. Mutlu-Pakdil et al. 2021); by examination of Figure 7 of G. A. Dooley et al. (2017), we estimate that ∼80% of an LMC-mass host's satellites should be within a radius of 90 kpc.

Data were obtained on two separate observing runs—the central, eastern, and western fields on 2016 February 9–10 and the northwest, northeast, southwest, and southeast fields on 2017 December 23–24. Skies were clear during both observing runs, with seeing between 0.″5 and 1.″4 (but typically better than 0.″9). To reach well below the TRGB at a distance of 3 Mpc, we observed sets of 10×300 s exposures in g band (called "HSC-G" at Subaru) and 10×120 s in i band ("HSC-I2"), as well as sequences of 5×30 s exposures in each filter to prevent saturation of bright sources. See Table 3 for a log of our HSC observations.

The data were processed using the Legacy Survey of Space and Time (LSST) Science Pipelines,[19] which are being developed to process data from the Vera C. Rubin Observatory's LSST (Ž. Ivezić et al. 2019). In particular, we used the weekly version of the Science Pipelines designated "w_2020_42" (i.e., the current version as of the 42nd week of 2020). A detailed description of the pipeline processing is presented in J. Bosch et al. (2018); see also J. Bosch et al. (2019). Processing includes instrument signature removal (e.g., bias correction, flat-fielding, etc.), a first round of source detection and matching to reference catalogs to derive photometric and astrometric calibration, point-spread function (PSF) fitting followed by refinements to the calibration, coaddition of overlapping frames, and finally detection and measurement of sources on the coadded images. The overall field covered by the data was assigned a single "tract," which was subdivided into a grid of 25×25 "patches" of 4000×4000 pixels each.

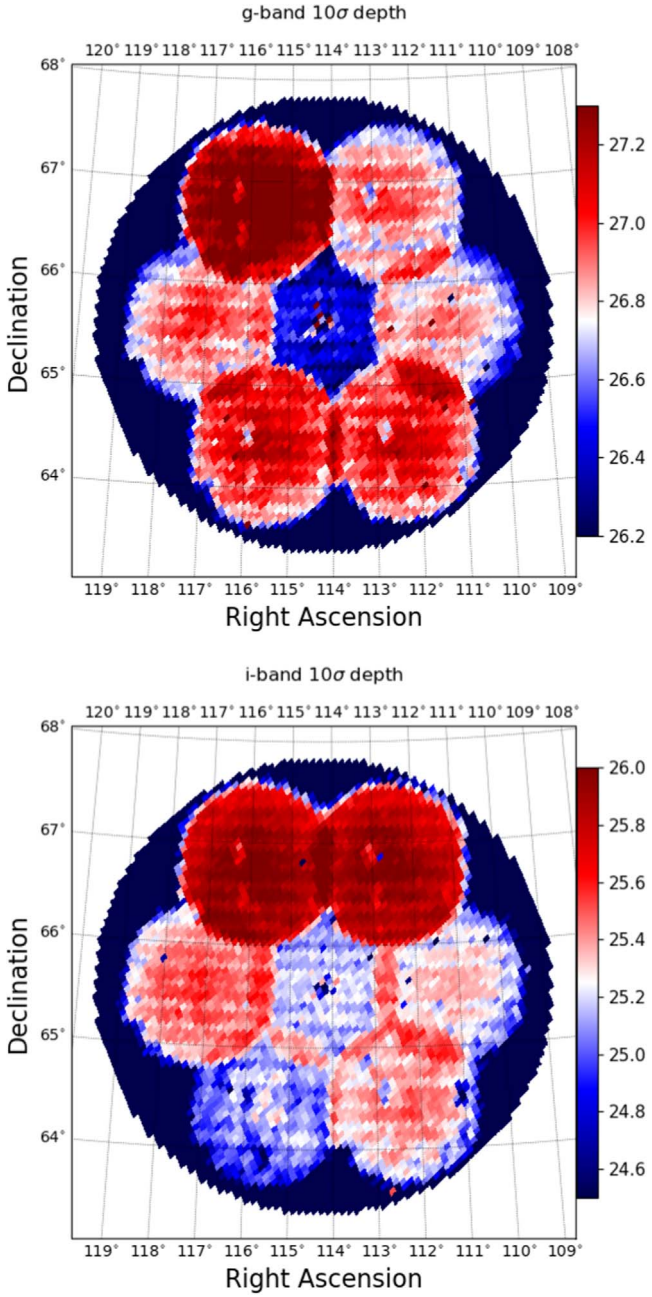

Figure 2. The final 10σ point-source depths as a function of position from our Subaru/HSC data set. The upper panel shows the g-band depth, and the lower panel depicts i-band depth. There is as much as ∼1 mag of variation in depth over the footprint, which is mostly due to different observing conditions (e.g., seeing; see Table 3) at the time the images were obtained.

The full observed region is shown in Figure 2. The seven HSC pointings are clearly distinguishable in these maps, as well as their overlapping regions at the edges. In Figure 2, the color code represents the 10σ point-source depth as a function of position (in g band in the upper panel and i band in the lower panel). There is ∼1 mag of variation in the depth as a function of position, most of which can be attributed to varying conditions under which the data were obtained.

[19] See https://pipelines.lsst.io/index.html.

Table 3
Subaru+HSC Observation Log and Field Completeness

Field Name	Filter	Date	Exp[a] (s)	seeing (arcsec)	50%[b] (mag)	90%[c] (mag)	10σ depth (mag)
NGC2403_CEN	HSC-G	2016-Feb-9	10×300	0.9–1.4	26.6	25.1	26.5
NGC2403_CEN	HSC-I2	2016-Feb-9	10×120	0.65–0.9	26.0	24.5	25.2
NGC2403_WEST	HSC-G	2016-Feb-10	10×300	0.6–0.75	27.7	26.4	26.9
NGC2403_WEST	HSC-I2	2016-Feb-9	10×120	0.65–0.8	26.3	24.8	25.4
NGC2403_EAST	HSC-G	2016-Feb-10	10×300	0.55–0.75	27.6	26.1	27.0
NGC2403_EAST	HSC-I2	2016-Feb-10	10×120	0.55–0.65	26.4	25.0	25.6
NGC2403_SE	HSC-G	2017-Dec-24	10×120	0.65–0.85	27.7	26.4	27.2
NGC2403_SE	HSC-I2	2017-Dec-24	10×120	0.55–0.75	26.1	24.6	25.3
NGC2403_SW	HSC-G	2017-Dec-24	10×120	0.6–0.85	27.7	26.2	27.2
NGC2403_SW	HSC-I2	2017-Dec-24	10×120	0.55–0.65	26.4	24.9	25.5
NGC2403_NE	HSC-G	2017-Dec-25	10×300	0.5–0.55	28.1	26.8	27.0
NGC2403_NE	HSC-I2	2017-Dec-25	10×120	0.5–0.6	26.9	25.5	26.0
NGC2403_NW	HSC-G	2017-Dec-25	10×300	0.5–0.7	27.8	26.2	27.0
NGC2403_NW	HSC-I2	2017-Dec-25	10×300	0.5–0.6	26.8	25.5	26.0

Notes.
[a] Total exposure time in seconds. We also took 5×30 s exposures in each field to increase the dynamic range at the bright end.
[b] Magnitude at which the data are 50% complete, based on artificial star tests.
[c] Magnitude at which the data are 90% complete.

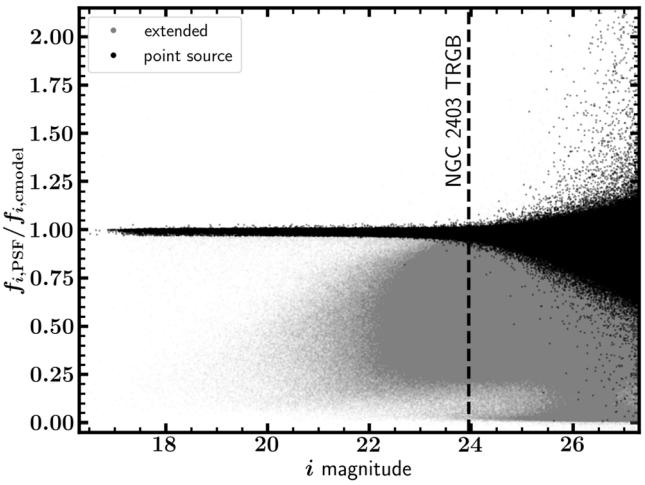

Figure 3. An illustration of our method for star/galaxy separation. The ratio of point-spread-function (PSF) and `cmodel` fluxes is plotted against the *i*-band PSF magnitude. Point-like objects (i.e., "stars") should have $f_{\mathrm{PSF}}/f_{\mathrm{cmodel}} \sim 1$, while extended objects have more flux in the galaxy model measurement, scattering them to $f_{\mathrm{PSF}}/f_{\mathrm{cmodel}} < 1$. Objects are classified as likely stars (highlighted in black in the diagram) if they are within 3% (accounting for their measurement errors) of unity in this figure.

Results presented throughout this work are based on forced PSF photometry performed on the coadded images in each filter. The photometric and astrometric calibrations used PanSTARRS-1 (E. F. Schlafly et al. 2012; J. L. Tonry et al. 2012; E. A. Magnier et al. 2013) as a reference catalog. All data presented here have been corrected for extinction based on the D. J. Schlegel et al. (1998) dust maps, using the coefficients from E. F. Schlafly & D. P. Finkbeiner (2011).

3.1. Star–Galaxy Separation

Figure 3 demonstrates our criteria for distinguishing point sources (i.e., "stars") from galaxies. The `cmodel` galaxy model fluxes should be equal to the PSF magnitudes for point sources, while the `cmodel` measurements capture the flux in the extended regions of resolved galaxies, whose fluxes thus diverge from PSF measurements of the same objects. We use the ratio of PSF to `cmodel` flux as a selection criterion to distinguish "point-like" sources from extended sources. Specifically, we select sources whose flux ratios are within ± 0.03 of unity (accounting for the uncertainties on their fluxes) in both the *g* and *i* bands. In Figure 3, the point sources selected in this way are black points, while sources classified as extended are shown as lighter gray points.

3.2. Point-source Completeness via Artificial Star Tests

To characterize the completeness of point-source detections in our images, we injected artificial stars into each patch of the coadded images. Artificial stars were randomly generated between magnitudes $20 < i < 28$ and with colors between $-1 < (g - i) < 2.5$, with weighting applied to generate more stars at fainter magnitudes than at the bright end. Positions were assigned randomly such that the stellar density of injected stars is on average $\sim 15\ \mathrm{arcmin}^{-2}$ throughout the entire observed field. The resulting images were then reprocessed in the same manner as the original processing, and the measurement catalog was matched (with a $0\farcs5$ matching radius) and compared to the input list of artificial stars. Note that we did not apply star/galaxy separation criteria in this analysis but concerned ourselves only with *detection* completeness.

Figure 4 shows the results from the artificial star tests in the northeast (NE) field. The upper panel shows the completeness in *g* (blue points) and *i* (red points) as a function of magnitude. For similar completeness curves in each of the seven fields, we fit a function of the form:

$$\eta(m) = \frac{A}{1 + \exp(\frac{m - m_{50}}{\rho})} \quad (1)$$

as in N. F. Martin et al. (2016, Equation (7)), where $\eta(m)$ is the completeness as a function of magnitude, A characterizes the plateau at bright magnitudes (typically near 1.0 as recovery of bright stars should be nearly complete), ρ characterizes the steepness of the falloff at the faint end, and m_{50} represents

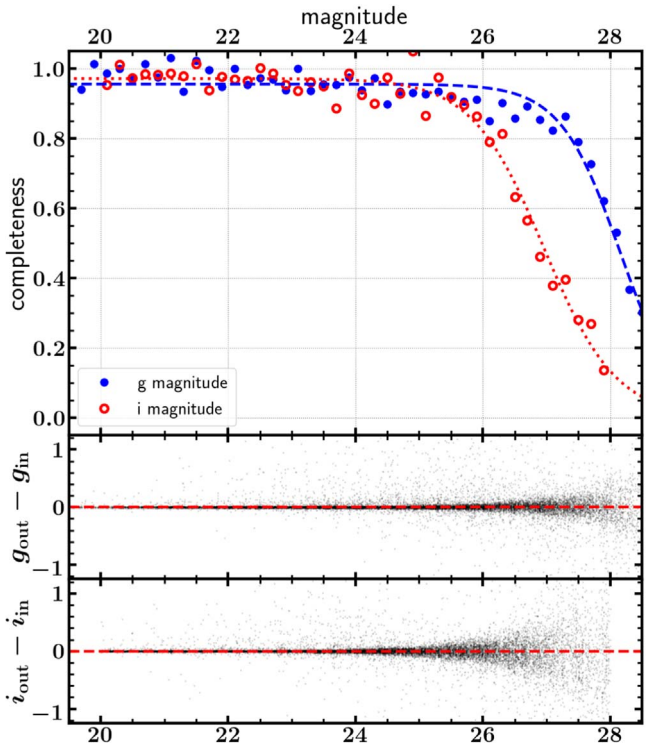

Figure 4. Point-source completeness based on artificial star tests (see Section 3.2) from the central 20′ of the NE field. Blue and red points represent the *g*- and *i*-band completeness, respectively. The overlaid lines are the fits of Equation (1) to the completeness values. The lower two panels compare the injected and measured magnitudes of artificial stars; there is no magnitude bias evident. The NE field is the deepest in both *g* and *i* bands of all our seven fields; the 50% and 90% completeness results from all fields are given in Table 3 along with the 10σ point-source depths.

magnitudes where 50% of the injected stars were recovered (i.e., the 50% completeness magnitude). Each 20′ radius field contains ∼18,000 artificial stars. The results from functional fits of Equation (1) to curves in each field similar to that in Figure 4 are summarized numerically in the 50% and 90% completeness columns in Table 3, where we also provide the median 10σ limiting magnitude derived from the maps in Figure 2. There is significant variation in the depth over the observed footprint, which must be accounted for when estimating our sensitivity to the faint dwarfs we seek to detect.

3.3. RGB Candidate Selection

Figure 5 demonstrates our adopted color–magnitude criteria for selecting candidate RGB stars at the distance of NGC 2403. We select stars that are consistent with being metal-poor RGB stars at or near the distance of NGC 2403 (i.e., roughly consistent with the isochrones overlaid on the CMDs in Figure 5) within a box in color–magnitude space. We choose a box rather than an isochrone filter because at the distance of NGC 2403, many stars in potential dwarf galaxies may have their fluxes contaminated by unresolved flux from the dwarf galaxy's stars below the detection limit (see, e.g., C. T. Garling et al. 2021) and thus scatter their colors and magnitudes by much more than the magnitude uncertainties estimated by automated measurement algorithms. Although the color and magnitude errors increase at the faint end, we choose to narrow the selection box to avoid as many as possible of the unresolved galaxies that dominate the number counts of objects

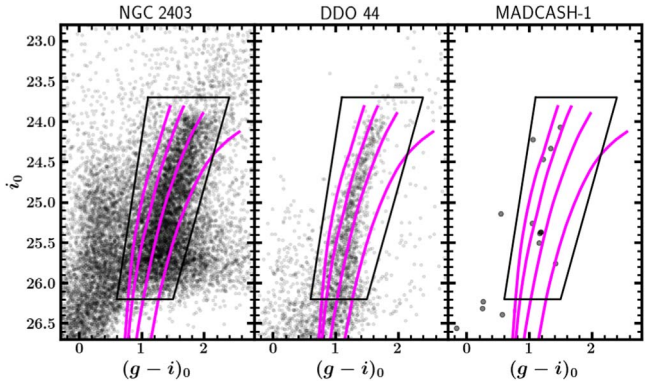

Figure 5. RGB star selection. Left: objects in an elliptical annulus between semimajor axes of $14 < a < 20'$ of the center of NGC 2403, at a position angle of 124° (Barker et al. 2012). Middle: between 2′ and 4′ from the center of DDO 44. Left: within 20″ of MADCASH-1. The black region in each panel outlines the RGB star selection. Isochrones in each panel are from A. Bressan et al. (2012), for metallicities of [M/H] = −2.0, −1.5, −1.0, and −0.5 and age 10 Gyr at a distance modulus of $m - M = 27.39$ (J. L. Carlin et al. 2016).

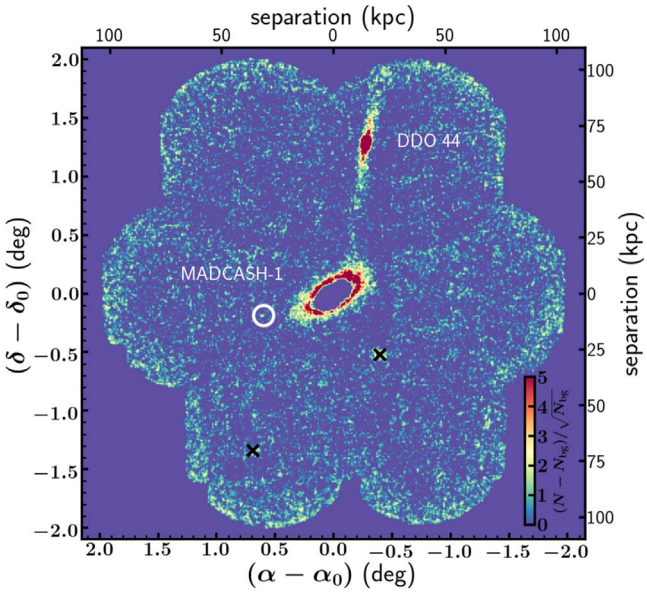

Figure 6. Map of selected RGB star candidates, shown here as the RGB number density "signal-to-noise" above the local background, $(N - N_{bg})/\sqrt{N_{bg}}$. DDO 44 and its tidal stream (J. L. Carlin et al. 2019) are prominent in the northern region of this panel. The faint satellite MADCASH-1 (J. L. Carlin et al. 2021) is visible (and circled in white) as a small overdensity to the east (and slightly south) of the main body of NGC 2403. The black cross (×) to the SE of NGC 2403 is MCG+11-10-022, and the one slightly SW is UGC-3894. The outskirts of NGC 2403are otherwise fairly featureless, with no obvious stellar streams or tidal debris structures visible. A rough estimate based on the background density and mean flux of RGB candidates suggests that these data should be sensitive to streams with surface brightnesses as faint as $\mu_V \sim 32$ mag arcsec^{-2}.

at the faint end. These selection criteria were chosen in part by trial and error, seeking the selection criteria that maximize the signal-to-noise of known dwarfs MADCASH 1 and DDO 44 (and its tidal stream; see J. L. Carlin et al. 2019).

Figure 6 shows a map of the signal-to-noise (i.e., significance above the background) of the surface density of RGB stars selected by our technique (a similar map that was shown in J. L. Carlin et al. 2019 was generated from an earlier processing of the data). NGC 2403 is visible in the center of the field, with very few other obvious features. The previously discovered MADCASH dwarf (J. L. Carlin et al. 2016) is

barely visible to the east (and slightly south) of the NGC 2403 disk. We mark two large and bright background galaxies that erroneously contribute to our RGB sample with black cross symbols. Otherwise, the only readily visible feature is the stellar tidal stream emanating from the massive satellite DDO 44, which can be traced nearly the entire ∼70 kpc projected distance between DDO 44 and NGC 2403. See J. L. Carlin et al. (2019) for more details about this stellar stream. From this map, we conclude that there are no other obvious stellar streams or tidal debris features in the halo of NGC 2403 to be followed up.

3.4. Search for Dwarf Galaxies

To search for candidate dwarf galaxies as overdensities of resolved stars, we adopt a simple approach. We first divide the footprint of our HSC observations into bins of 1.′0 on a side, which corresponds to ∼870 pc at the distance of NGC 2403. For each bin, we count the number of point sources within the RGB selection box—this constitutes the signal within each bin. The local background level is estimated by extracting the number of candidate RGB stars in bins whose centers lie in an annulus spanning a radius of 2–5 times the bin size (i.e., 2′–5′) from the bin, then scaling this number to account for the different areas of the annulus and the bin. Annuli that are only partially within the observational footprint (i.e., at the outer edge of the coverage) are corrected for the fraction of the annulus that is missing. Partial annuli are also necessary near the center of NGC 2403, where the extremely high number counts of stars would create artificially high background values (we also excluded bins within 15′ of the center of NGC 2403 from our search). Bins with number counts that are higher than the local background by more than 3.5 times the standard deviation of the counts in the background bins are considered candidate detections.

This search yields a total of 227 candidate overdensities. Of those, 42 are associated with the main body of NGC 2403 and are thus excluded from further consideration. Another 36 detections are associated with DDO 44 and its tidal stream; these are also removed from the sample, leaving 149 candidates for more detailed examination. We generated diagnostic plots as seen in the Appendix in Figures 11 through 17 for all candidates and examined each of them for evidence of a dwarf galaxy. The visual examination is critical, as any one of the panels (color–magnitude diagram (CMD), spatial distribution, radial density profile, image, and LF) can contain features suggesting the presence of a candidate dwarf. Take, for example, the previously known dwarf MADCASH 1 (J. L. Carlin et al. 2016), whose diagnostic plots are seen in Figure 13. This candidate's RGB stars roughly delineate a metal-poor RGB in the CMD, the stars of which are concentrated in the spatial plot, and are visible in the image (including some unresolved, low-surface-brightness emission), and the LF clearly differs from that of the background region. The candidate in Figure 14, on the other hand, shows no clear feature in the image or the spatial distribution, and its stars do not lie along a sequence consistent with being (and having the LF of) an RGB at the distance of NGC 2403. This candidate is thus an obvious false detection.

From the 149 candidates we examined, we identified only the known dwarf MADCASH 1 as a worthwhile candidate. Some candidates have enticing features in the diagnostic plots, but none make a convincing enough case to be considered bona fide dwarfs. It thus appears that the only NGC 2403 satellites detected in our data set are MADCASH-1 and DDO 44.

4. Completeness via Artificial Dwarf Galaxy Tests

To characterize our sensitivity to dwarf galaxies as a function of position, luminosity (M_V), and size (r_{half}; and by extension, surface brightness), we generate simulated dwarf galaxies, inject them into the images, and rerun the detection and measurement pipelines. Both our search for overdensities of RGB stars and the injected synthetic dwarfs focused on old, metal-poor stellar populations. This is a reasonable assumption given the fact that even dwarfs with recent star formation (or intact gas reservoirs) formed the majority of their stellar mass at early times (e.g., D. R. Weisz et al. 2011) and should thus be detectable via their old, metal-poor RGB stars.

The dwarfs were created by sampling Padova isochrones (A. Bressan et al. 2012) fixed at a 10 Gyr age and low metallicity ([Fe/H]= −2.0), with a G. Chabrier (2001) log-normal LF. We sampled in luminosity between $-9.5 < M_V < -6.0$ in 0.5 mag increments and in surface brightness (within r_{half}) spanning $23 < \mu_V < 34$ mag arcsec^{-2} in increments of 0.5 mag arcsec^{-2} (we implicitly assume that brighter dwarfs around NGC 2403 would have been detected in prior work). Dwarfs were simulated with H. C. Plummer (1911) distributions, with r_{half} implied by the combination of luminosity and surface brightness. Dwarfs were placed at a distance of 3.0 Mpc. To reduce the computational burden, simulated stars fainter than $r = 33$ mag were removed; at 3.0 Mpc, this cut removes a few percent of the total flux of the injected dwarfs, but we confirmed via inspection of the images that the effect was not visually noticeable. We randomly position between 2 and 5 dwarfs in each 4000 × 4000 pixel "patch" (varying the number of inserted dwarfs per patch to avoid predictable results). Dwarfs are injected as groups of individual stars using the version of `Synpipe` (S. Huang et al. 2018) that was integrated into the LSST science pipelines at the time the NGC 2403 data were processed. Example dwarf galaxy injections into the image-level data are shown in Figure 7, along with the actual appearance of MADCASH-1 for comparison.

A total of 3139 artificial dwarfs were injected into the images over two separate runs; this was accomplished by randomly generating between two and five artificial dwarfs per 4k × 4k "patch" for each of the 394 patches in the coadded image data (the maximum of five dwarfs per patch was chosen to avoid overlapping of injected dwarfs). The data were fully reprocessed and the dwarf search code run on the resulting catalogs. Dwarf detection completeness results are seen in Figure 8, where each bin in the luminosity–size plane had ∼40 artificial dwarfs injected. The completeness in each bin is simply the number detected by our algorithm divided by the total number injected in that bin. For context, we overlay known nearby dwarf galaxies from the Local Volume Database.[20] Our analysis shows that we are nearly complete (i.e., $\gtrsim$80% detected) for dwarfs at $M_V < -7.5$ and $\mu_V \lesssim 30$ mag arcsec^{-2}, with sensitivity extending as faint as $M_V = -6.5$. As shown in Figure 2, there is significant variation in depth over the observed field of view, such that Figure 8 represents an average completeness over the full data set. Thus, a conservative estimate of the faintest dwarf to which we are reliably sensitive is $M_V \sim -7.5$.

5. Discussion and Conclusions

Figure 9 shows the LF of NGC 2403 dwarf satellites, which consists of only two systems: DDO 44 ($M_V = -12.9$;

[20] https://github.com/apace7/local_volume_database

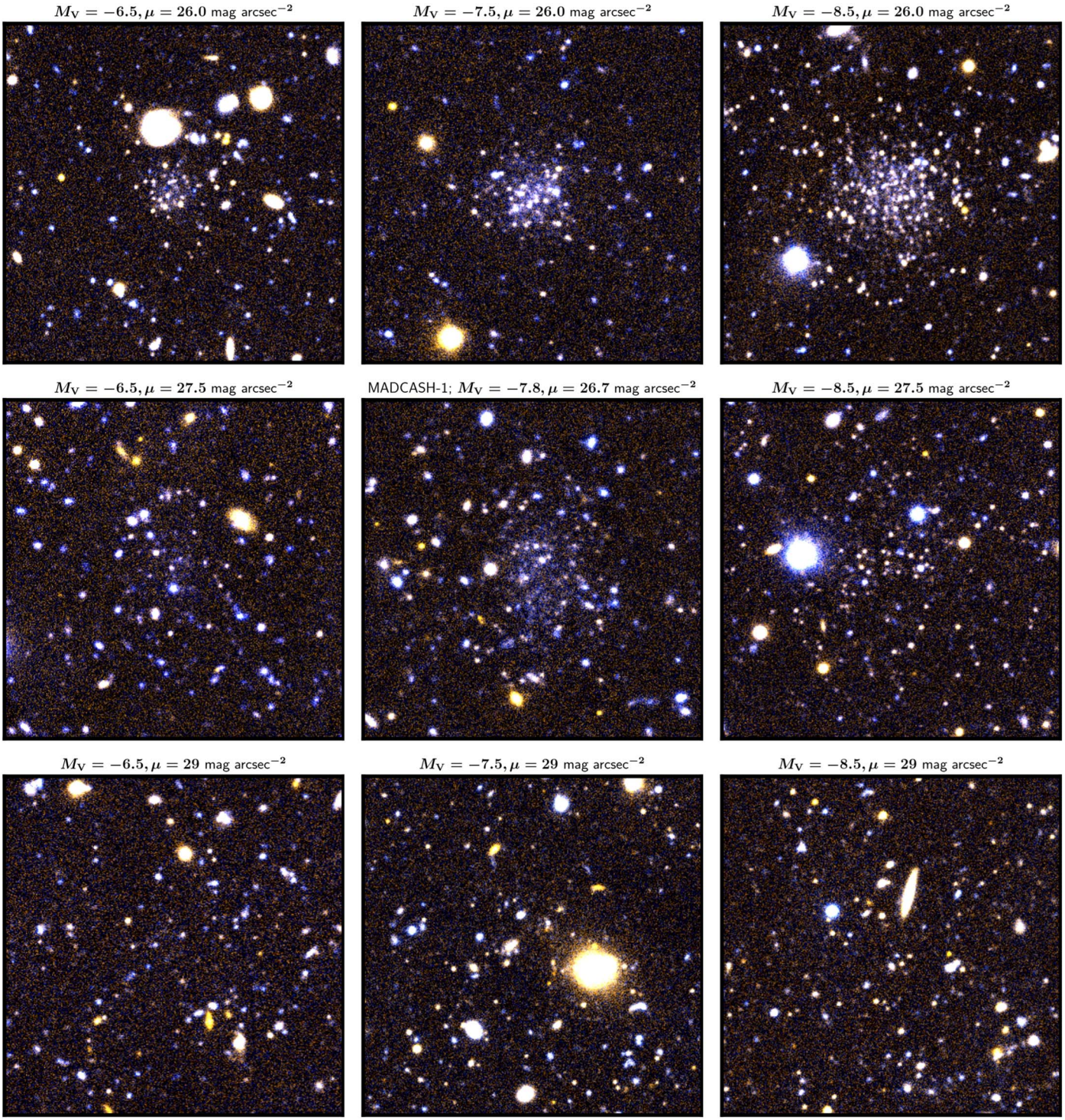

Figure 7. Example images of synthetic dwarfs that were injected into the images to measure our recovery rate. Images are 1′ on a side, corresponding to a projected physical width of ∼870 pc at a distance of 3 Mpc. Each row shows dwarfs with fixed values of surface brightness, with μ = 26.0, 27.5, 29.0 mag arcsec^{-2} in the top, middle, and bottom rows. From left to right, injected dwarfs have $M_V = -6.5, -7.5, -8.5$ in each row. However, the middle panel has been replaced with an image of the MADCASH-1 dwarf, which has μ = 26.7 mag arcsec^{-2} and $M_V = -7.8$. All of the dwarfs shown in this figure were recovered by our search. Our injected dwarf recovery fractions for similar dwarfs were 23%, 34%, and 63% for the top panels; 26% and 67% for the left- and right-hand panels in the middle row; and 26%, 57%, and 72% for the dwarfs in the bottom row. The bin in Figure 8 corresponding to MADCASH-1 had a recovery rate of 74%.

J. L. Carlin et al. 2019) and MADCASH-1 ($M_V = -7.8$; J. L. Carlin et al. 2021); the properties of these dwarfs are summarized in Table 4. For comparison, we overlay the predicted satellite population for an LMC-mass host as derived by I. M. E. Santos-Santos et al. (2022) as a blue filled region and from G. A. Dooley et al. (2017) as an orange shaded region. Both of these predicted satellite LFs were corrected for the dwarf detection completeness of our HSC data as estimated in Section 4 and Figure 8. We did not incorporate the full dependence of our dwarf sensitivity on M_V and $r_{\rm half}$ but rather interpolated along the locus occupied by Milky Way (MW) dwarfs in the M_V–$r_{\rm half}$ plane (as measured by C. M. Brasseur et al. 2011). The predicted LFs in

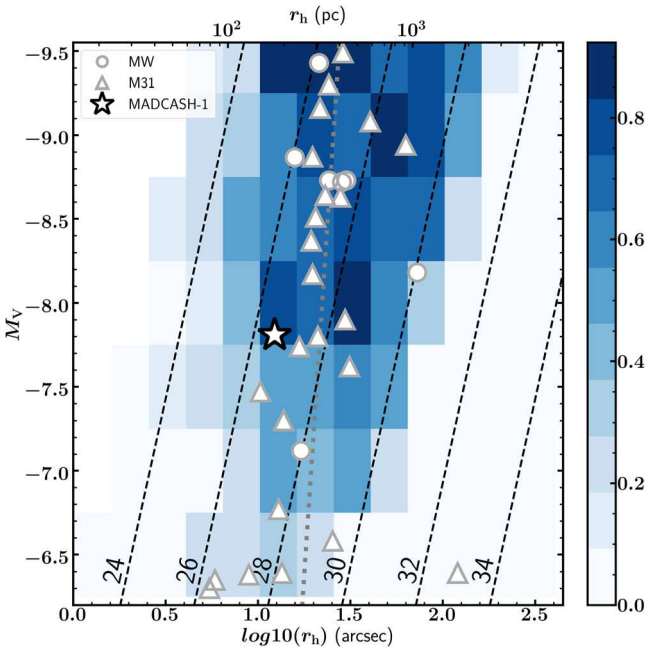

Figure 8. Completeness of dwarf galaxy detection based on the injection of >3000 artificial dwarfs (>40 per bin in the figure). For comparison, we show the positions of known Milky Way (circles) and M31 (triangles) dwarfs from the Local Volume Database. NGC 2403's satellite MADCASH-1 is shown as a large star with black outline; DDO 44 is much brighter than the upper limit we explored with artificial dwarfs and thus outside the boundaries of this figure. Diagonal lines represent constant surface brightness values, ranging from 24 to 32 mag arcsec^{-2}. The gray dotted line is the interpolated M_V–r_{half} relation from C. M. Brasseur et al. (2011), which we use to extract the LF corrections applied to Figure 9. Our data set and search sensitivity should recover most typical dwarfs brighter than $M_V < -7.0$ and $\mu_V \lesssim 30$ mag arcsec^{-2} and some fraction at even fainter absolute magnitudes.

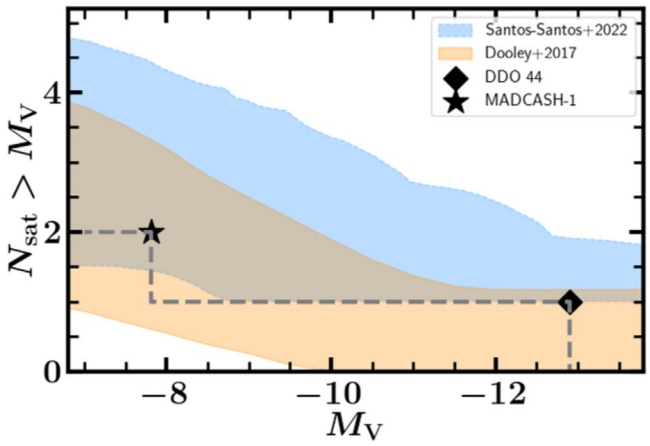

Figure 9. Satellite LF of NGC 2403. The filled bands represent predicted satellite populations for LMC-mass hosts from I. M. E. Santos-Santos et al. (2022, blue) and G. A. Dooley et al. (2017, orange). The shaded regions for both comparisons represent the 1σ variation in the number of satellites over the model realizations. The predicted LFs have been corrected for dwarf detection completeness as well as a volume correction to account for the observational incomplete coverage of the virial volume (see Section 5 for details).

Figure 9 were then simply scaled based on the dwarf sensitivity at each M_V value that was extracted along the C. M. Brasseur et al. (2011) size–luminosity curve. Finally, we applied an additional reduction by a factor of 0.8 at all luminosities to account for our incomplete coverage of the virial radius of NGC 2403. This factor was estimated from Figure 7 of G. A. Dooley et al. (2017), which shows the cumulative number of satellite dwarfs as a function of radius from an LMC-mass host; our complete coverage to ~90 kpc should encompass ~80% of the NGC 2403 satellites.

In Figure 9, we compare the properties of our observed NGC 2403 satellites to two ΛCDM-based predictions for satellite populations of LMC-mass hosts. The orange shaded region represents the 1σ scatter in predicted satellites from the work of G. A. Dooley et al. (2017), which is based on the Caterpillar simulations (B. F. Griffen et al. 2016) and the stellar mass–halo mass relation of S. Garrison-Kimmel et al. (2017). The blue filled region shows predicted satellites for LMC analogs from I. M. E. Santos-Santos et al. (2022), whose work was based on the highest-resolution models from the APOSTLE simulations suite (A. Fattahi et al. 2016). The region we include here for comparison corresponds to the "cutoff" model from I. M. E. Santos-Santos et al. (2022), which predicts far fewer satellites than a standard power law. The predictions from both models align well with the two observed satellites of NGC 2403.

The LMC itself, while known to have many satellites, has only one confirmed satellite (the SMC) that is not an ultrafaint dwarf (i.e., brighter than $M_V \sim -7.5$; see, e.g., E. Patel et al. 2020), so the LMC's satellite population placed in Figure 9 would be a single line at $N = 1$ (though with some uncertainty given our limited ability to kinematically confirm or refute associations between classical dwarfs and the LMC). M33, a massive companion of the Andromeda galaxy (M31), has roughly the same stellar mass as the LMC. Its inner halo (within $r \sim 50$ kpc) has been searched extensively for satellites with the PANDAS survey (N. F. Martin et al. 2009), with one of the candidates (And XXII; $M_V = -6.5$) spectroscopically confirmed to be a likely satellite of M33 (S. C. Chapman et al. 2013). Recently, Pisces VII/Tri III was discovered (D. Martínez-Delgado et al. 2022) at a projected distance of ~70 kpc from M33 and subsequently confirmed as an $M_V = -6.0$ satellite of M33 by M. L. M. Collins et al. (2024). These dwarfs as well as the candidate ultradiffuse galaxy Tri IV (I. Ogami et al. 2024, $M_V = -6.4$), are shown as open black triangles in Figure 10, which places the satellites of NGC 2403 in context with the LMC and other nearby MC analogs (as well as the MW and M31). It is intriguing that all known or candidate M33 satellites thus far are ultrafaint dwarfs though a deeper search extending to the virial radius of M33 would need to be carried out to confirm that no brighter satellites of M33 are present.

The dwarf satellite populations of MC analogs *beyond* the Local Group have not yet been quantitatively explored in the way we have for NGC 2403 in this work. However, a number of MC-mass systems have known dwarf satellites. We show these in context with satellites of the LMC, M33, and the MW and M31 in a luminosity–size diagram in Figure 10.[21] NGC 3109, a galaxy with roughly half the stellar mass of the SMC that resides at the outskirts of the Local Group ($D \sim 1.3$ Mpc), has two known satellites (for a comprehensive characterization of the census and its sensitivities, see A. Doliva-Dolinsky et al. 2024, in preparation). Both Antlia ($M_V = -10.4$; M. E. Sharina et al. 2008) and Antlia B ($M_V = -9.7$; D. J. Sand et al. 2015) have H I gas (D. G. Barnes & W. J. G. de Blok 2001; J. Ott et al. 2012)

[21] We do not include potential satellites of LMC analog NGC 300 from D. J. Sand et al. (2024) in Figure 10 because it is unclear which of the three dwarfs presented in that work are actually satellites of NGC 300 and which are foreground or background systems (and thus isolated and intriguing in their own right). Follow-up studies will be necessary to assess the association of these dwarfs with NGC 300.

Table 4
Properties of the Satellite System of NGC 2403

Galaxy	R.A. (deg)	Decl. (deg)	$D_{\rm TRGB}$ (Mpc)	M_V (mag)	$r_{\rm half}$ (pc)	$r_{\rm half}$ (arcsec)	M_* ($M_\odot$)	$D_{\rm proj}$ (kpc)	References
(1)	(2)	(3)	(4)	(5)	(6)	(7)	(8)	(9)	(10)
DDO 44	113.5479	66.8797	2.96 ± 0.1	-12.9	740 ± 20	52 ± 2	2×10^7	~70	(1), (2), (3)
MADCASH-1	115.6642	65.4167	$3.41^{+0.24}_{-0.23}$	-7.81 ± 0.18	179^{+30}_{-28}	10.8 ± 1.0	$(1.8 \pm 0.3) \times 10^5$	~35	(4), (5)

Notes. Column (1): galaxy name; column (2): R.A. (J2000.0); column (3): decl. (J2000.0); column (4): TRGB distance; column (5): absolute V-band magnitude; column (6): physical half-light radius; column (7): half-light radius on the sky; column (8): stellar mass, estimated assuming $M_*/L_V = 1.6$, a typical value for dSphs (J. Woo et al. 2008); column (9): projected distance from NGC 2403; column (10): references.
References: (1) A. B. Whiting et al. (2007), (2) H. Jerjen et al. (2001), (3) J. L. Carlin et al. (2019), (4) J. L. Carlin et al. (2016), (5) J. L. Carlin et al. (2021).

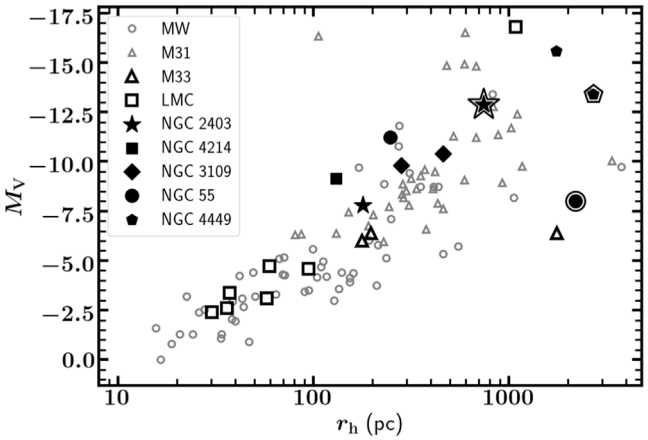

Figure 10. Luminosity (M_V) vs. half-light radius (r_h) for known satellites of MC-mass hosts in the Local Volume. Open gray symbols show the Milky Way and M31 satellites, with open black squares and triangles depicting (candidate) LMC and M33 satellites, respectively. Solid black symbols represent dwarf satellites of nearby ($1 < D < 4$ Mpc) MC-mass host galaxies for NGC 2403 (MADCASH 1, DDO 44); NGC 4214 (MADCASH 2); NGC 3109 (Antlia, Antlia B); NGC 55 (NGC 55-dw1, ESO 294-G010); and NGC 4449 (NGC 4449B, DDO 125). Symbols that are outlined are dwarfs that are known to be tidally disrupting.

and small amounts of recent star formation (K. B. W. McQuinn et al. 2010; J. R. Hargis et al. 2020) but have likely been quenched via starvation due to outflows related to that star formation (C. T. Garling et al. 2024). Until recently, the LMC stellar mass galaxy NGC 55 ($D \sim 2$ Mpc) had only a single known satellite, with $M_V \approx -11$. M. McNanna et al. (2024) unveiled another NGC 55 satellite in a search of Dark Energy Survey data. This dwarf, NGC 55-dw1, has $M_V = -8.0$ but is unusually large for its luminosity. Its half-light radius of ~2.2 kpc makes it the largest known dwarf galaxy fainter than $M_V = -9$, suggesting that its size may be inflated due to a recent tidal interaction with NGC 55. Likewise, the young stellar population identified in Hubble Space Telescope imaging of MADCASH 2, an $M_V = -9.2$ satellite of NGC 4214 (J. L. Carlin et al. 2021), a nearby ($D = 2.9$ Mpc) galaxy with stellar mass roughly twice that of the SMC, could be interpreted as evidence for recent tidal interaction between MADCASH 2 and NGC 4214. Another LMC analog, NGC 4449 ($D \sim 3.8$ Mpc), has a known disrupting dwarf companion (D. Martínez-Delgado et al. 2012; R. M. Rich et al. 2012) with stellar mass comparable to the (MW satellite) Fornax dSph. This particular satellite is the only dwarf satellite of an MC analog host with a spectroscopically measured velocity and metallicity (E. Toloba et al. 2016). E. D. Jahn et al. (2022) showed that tidal structures may be common around many MC-mass galaxies; it seems we are seeing evidence of this in the sample that has been revealed recently.

Clearly, comprehensive searches such as the one reported here for NGC 2403 will uncover numerous dwarf satellites, as well as tidal debris and disrupting dwarfs. This work provides tantalizing hints at the treasures we will uncover with the Vera C. Rubin Observatory's upcoming LSST (Ž. Ivezić et al. 2019; B. Mutlu-Pakdil et al. 2021), which will reach comparable photometric depths over the entire southern sky.

Acknowledgments

We thank the referee for insightful comments that helped improve the manuscript. We acknowledge support from the following NSF grants: AST-1816196 (J.L.C.); AST-1814208 (D.C.); and AST-1813628 (A.H.G.P and C.T.G.). Research by A.D.D. is supported by NSF grant AST-1814208. D.J.S. acknowledges support from NSF grant AST-2205863. K.S. acknowledges support from the Natural Sciences and Engineering Research Council of Canada (NSERC).

This research has made use of NASA's Astrophysics Data System, and `Astropy`, a community-developed core Python package for Astronomy (A. M. Price-Whelan et al. 2018).

The Pan-STARRS1 Surveys have been made possible through contributions of the Institute for Astronomy, the University of Hawaii, the Pan-STARRS Project Office, the Max-Planck Society and its participating institutes, the Max Planck Institute for Astronomy, Heidelberg and the Max Planck Institute for Extraterrestrial Physics, Garching, The Johns Hopkins University, Durham University, the University of Edinburgh, Queen's University Belfast, the Harvard-Smithsonian Center for Astrophysics, the Las Cumbres Observatory Global Telescope Network Incorporated, the National Central University of Taiwan, the Space Telescope Science Institute, the National Aeronautics and Space Administration under grant No. NNX08AR22G issued through the Planetary Science Division of the NASA Science Mission Directorate, the National Science Foundation under Grant AST-1238877, the University of Maryland, Eotvos Lorand University (ELTE), and the Los Alamos National Laboratory.

Facilities: Subaru, PS1.

Software: `astropy` (T. P. Robitaille et al. 2013; A. M. Price-Whelan et al. 2018), `Matplotlib` (J. D. Hunter 2007), `NumPy` (S. van der Walt et al. 2011), `Topcat` (M. Taylor 2005).

Appendix
Example Diagnostic Plots from Dwarf Search

Examples of the diagnostic plots we used to examine candidate dwarf detections are seen in Figures 11 through 17. Our dwarf search algorithm produced multiple detections of

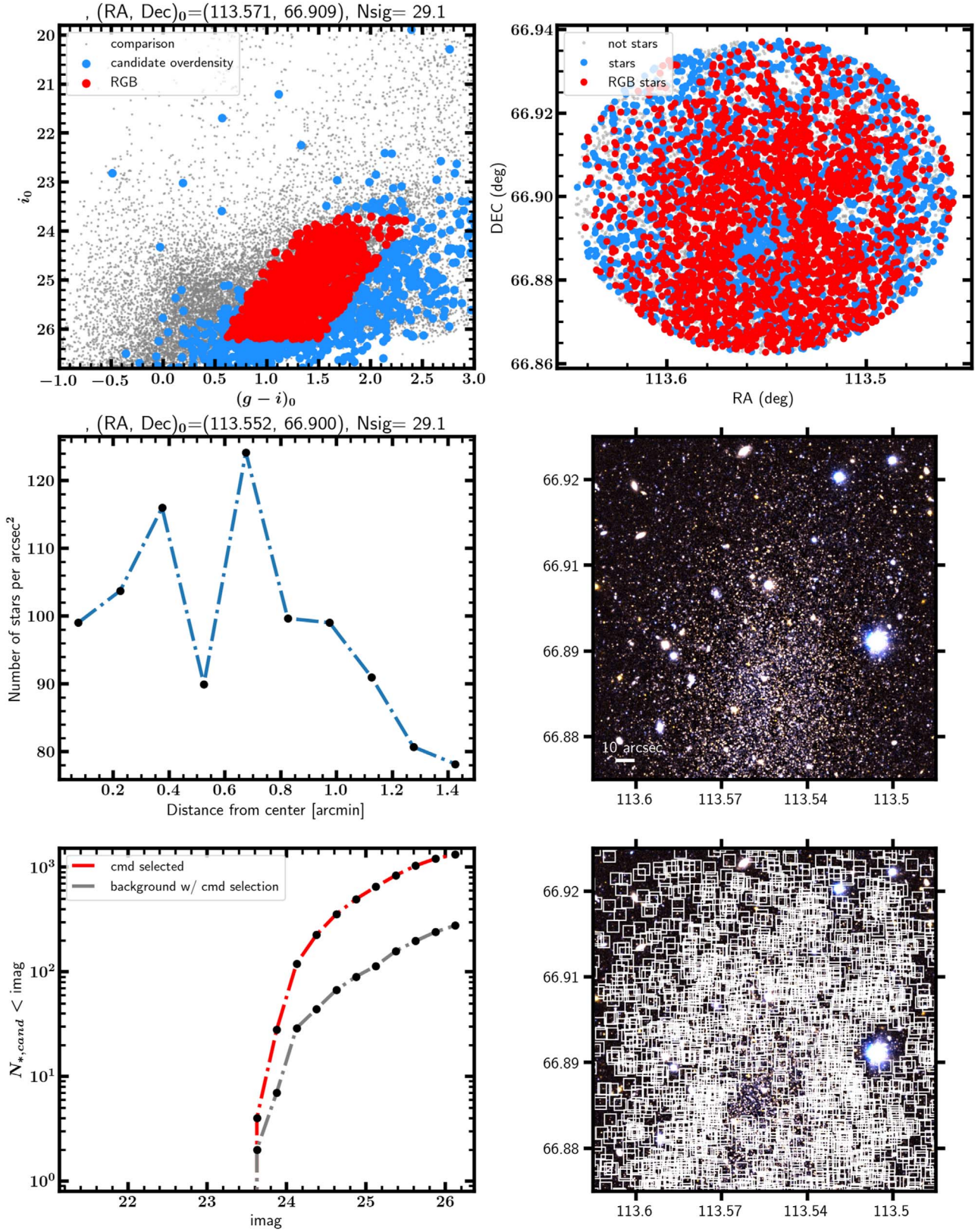

Figure 11. Example diagnostic plot of a detection of (a portion of) DDO 44. The upper left panel shows a CMD, with candidate RGB stars highlighted in red and all point sources within a $1'$ radius shown in blue. The upper right panel displays the spatial distribution of sources, using the same color-coding. In the middle left plot, we show a radial surface density plot (note that the center may not be properly located on the center of the overdensity, as we have not refined the measurements at this point). The middle right panel shows a color image of the region, and the lower right panel is the same image with RGB stars overlaid. In the lower left plot, we show an "LF" of candidate RGB stars; if a dwarf stellar population is present, one would expect the candidate dwarf (in red) to have a different LF than the neighboring field stars (shown in gray), as it does here for DDO 44.

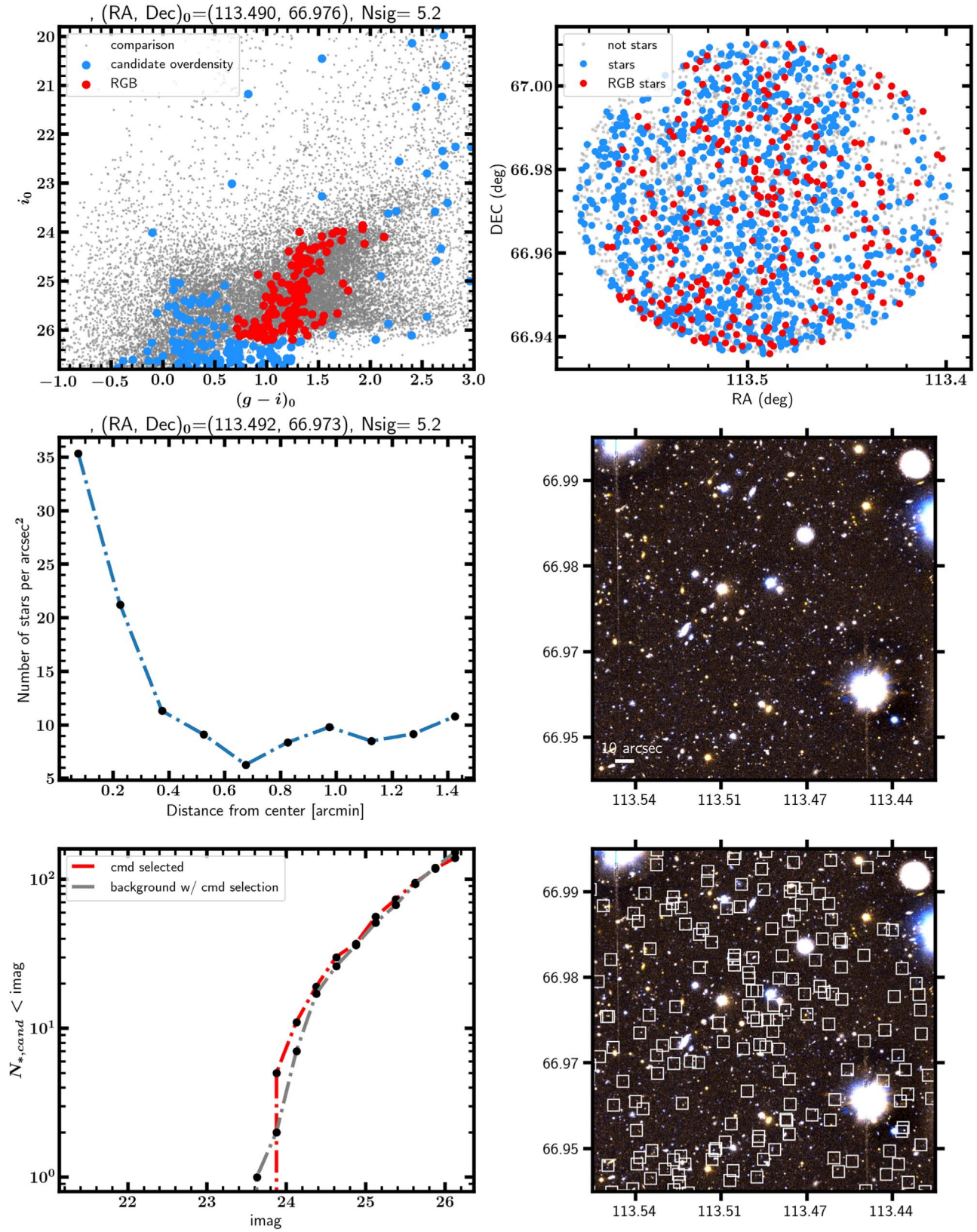

Figure 12. Example diagnostic plot. This particular plot shows a portion of the DDO 44 stream, detected a few arcminutes from the center of DDO 44. The RGB is clearly visible in the upper left panel (CMD).

DDO 44 and parts of its tidal stream. An example of a DDO 44 detection is shown in Figure 11, and a portion of its tidal stream (identified via its coordinates that place it on the stream track) is seen in Figure 12. While the main body of luminous dwarf DDO 44 is clearly visible in all panels of the diagnostic plot, the stream is only clearly identifiable via its signature in the

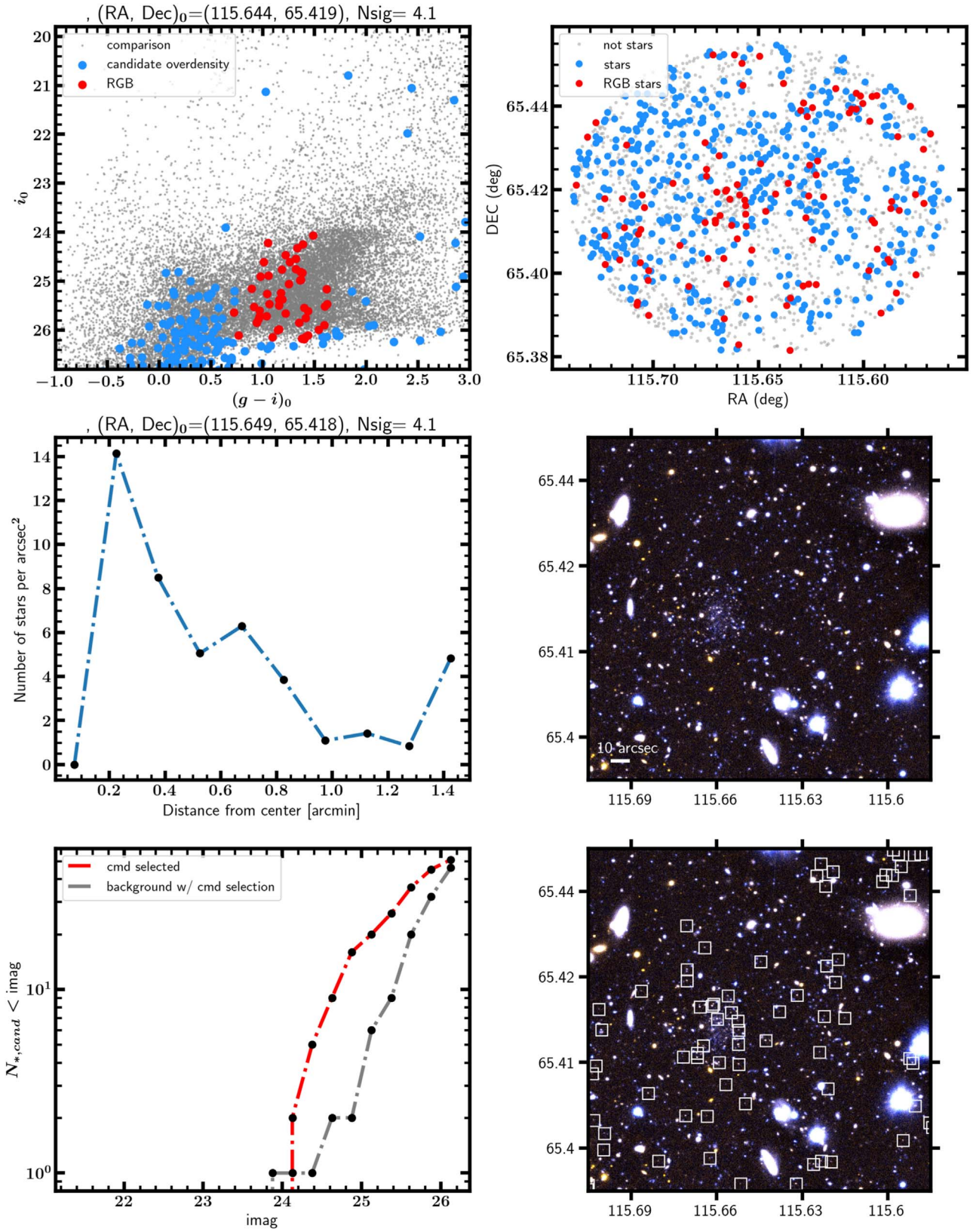

Figure 13. Example diagnostic plot showing the detection of MADCASH-1, the previously known ultrafaint dwarf near NGC 2403. Panels are as in Figure 11. The metal-poor RGB of MADCASH-1 is discernible in the CMD (upper left panel), but one can see in the images that the system is semiresolved, and thus, only a small number of stars are detected in the region of the semiresolved "fluff" around this ultrafaint dwarf.

CMD. The diagnostic plot for the much fainter known dwarf MADCASH-1 is seen in Figure 13. A metal-poor RGB sequence is visible in the CMD, and the presence of a dwarf is easily corroborated by looking at the images, where a semiresolved dwarf is prominently seen slightly to the left of the image center.

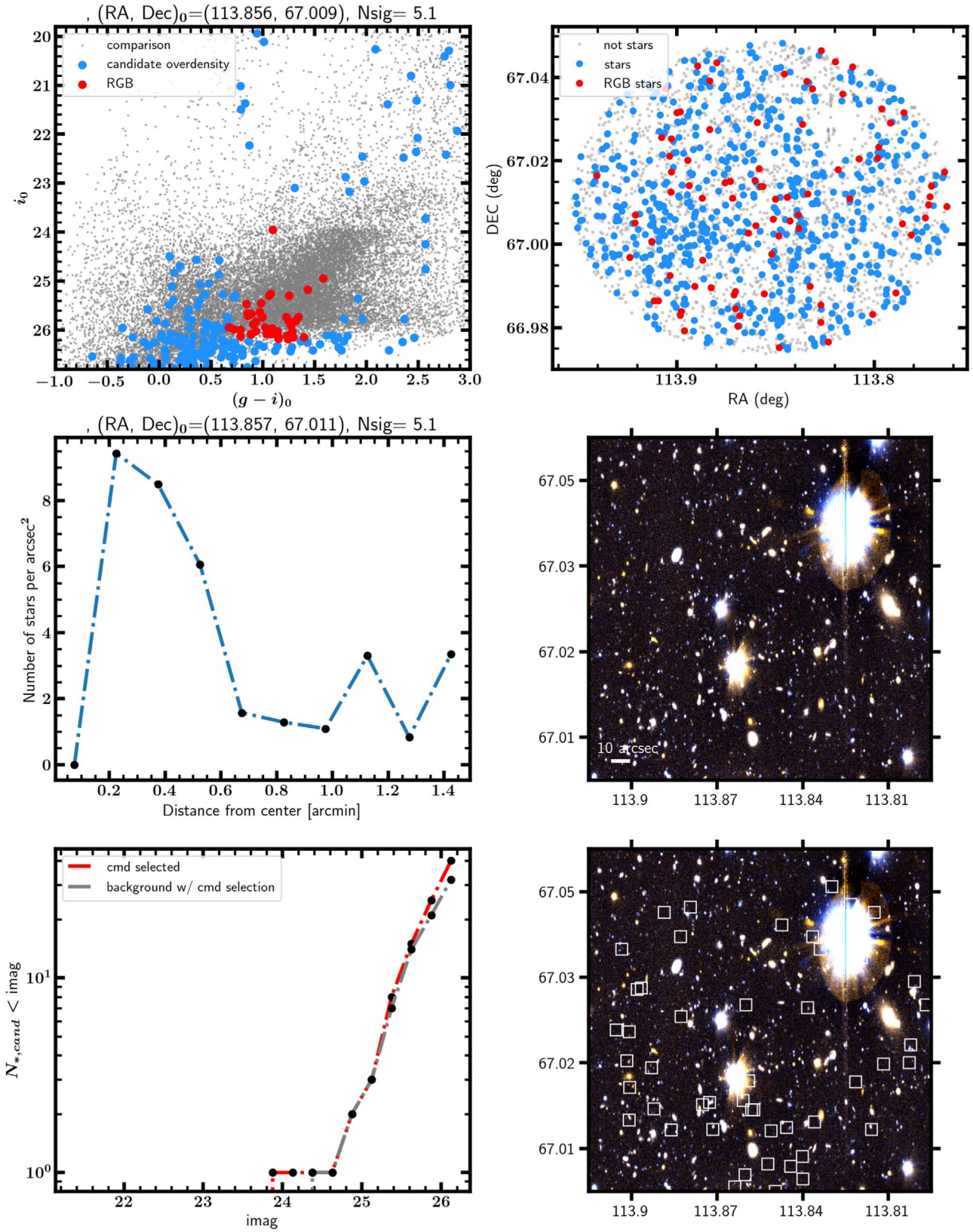

Figure 14. Example diagnostic plot showing a candidate detection that is highly unlikely to be a dwarf galaxy associated with NGC 2403. Note that the LF of objects detected within the RGB box does not resemble a typical LF for stars in a dwarf galaxy but rather looks as if it was drawn from the (unresolved) background galaxy population.

Figure 14 shows a fairly common type of false detection from our dwarf search. While a statistical "excess" over background was identified by the algorithm, it is clear from the CMD (upper left panel) that the sources contributing to the detection are predominantly faint, unresolved galaxies at the faintest end of the RGB selection box. A contributing factor to

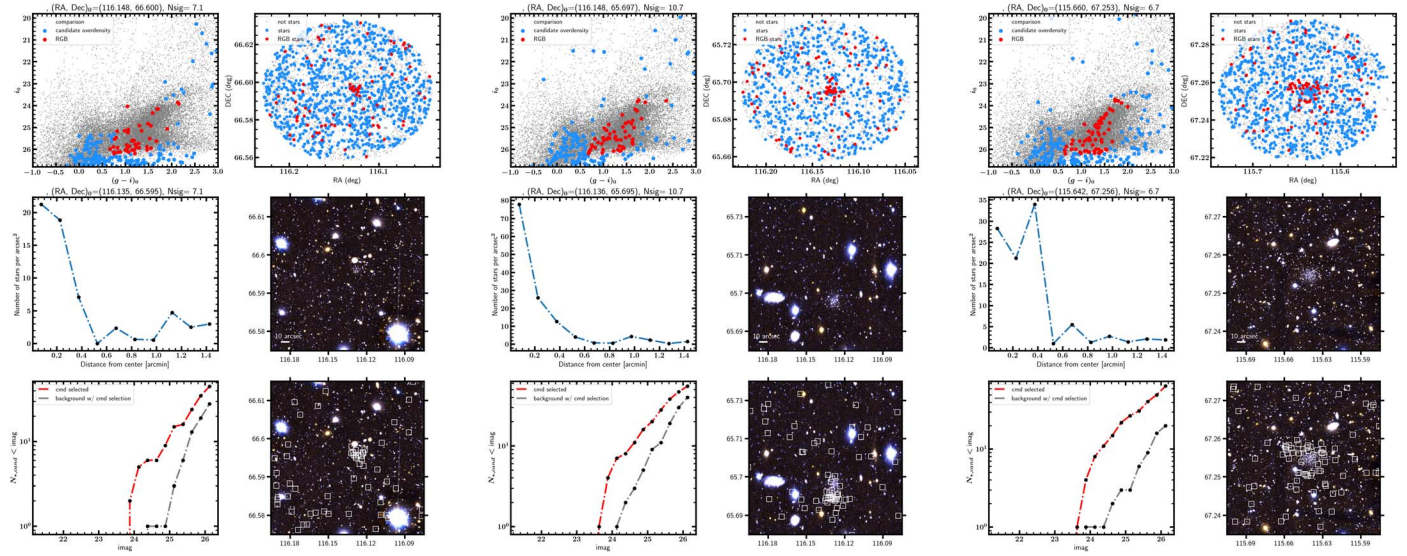

Figure 15. Diagnostic plots for the dwarfs from the top row of Figure 7, with surface brightnesses of ∼26.0 mag arcsec^{-2}, and (from left to right) $M_V \approx -6.5$, -7.5, and -8.5.

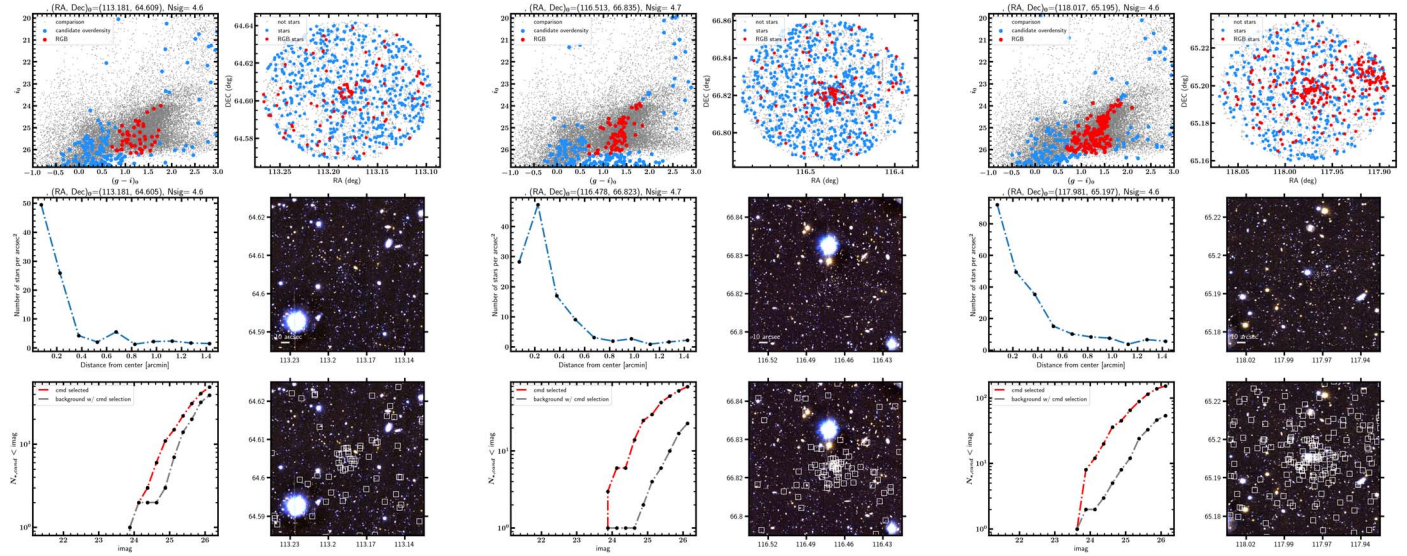

Figure 16. Diagnostic plots for the dwarfs from the middle row of Figure 7, with surface brightnesses of ∼27.5 mag arcsec^{-2}, and (from left to right) $M_V \approx -6.5$, -7.5, and -8.5. Note that the middle panel in Figure 7 was replaced with an image of MADCASH-1; the middle set of diagnostic plots above are for a synthetic dwarf with $M_V \approx -7.5$ and $\mu \approx 27.5$ mag arcsec^{-2}.

false detections like this is often the presence of a bright star or galaxy nearby. Such bright sources create "holes" where there are no sources detected, thus artificially decreasing the background counts and causing the appearance of an overdensity where there is none.

Finally, we include diagnostic plots for the synthetic dwarfs from Figure 7. Figures 15, 16, and 17 show the relevant plots for the top, middle, and bottom rows of Figure 7, respectively. These figures (and the fact that all of these synthetic dwarfs were detected by our search algorithm) demonstrate that our search should have been sensitive to dwarfs as faint as $M_V = -6.5$ to surface brightnesses as low as 29 mag arcsec^{-2}. Although the $\mu \approx 29$ mag arcsec^{-2} synthetic dwarfs in Figure 17 are not visible in the images, they are identifiable via their metal-poor RGB in the CMDs and as spatial overdensities. All of the synthetic dwarfs in these figures are readily identifiable in their diagnostic plots; thus, the fact that we did not identify any similarly obvious candidates among the candidates in our Subaru/HSC data suggests that no legitimate dwarfs were present in the data.

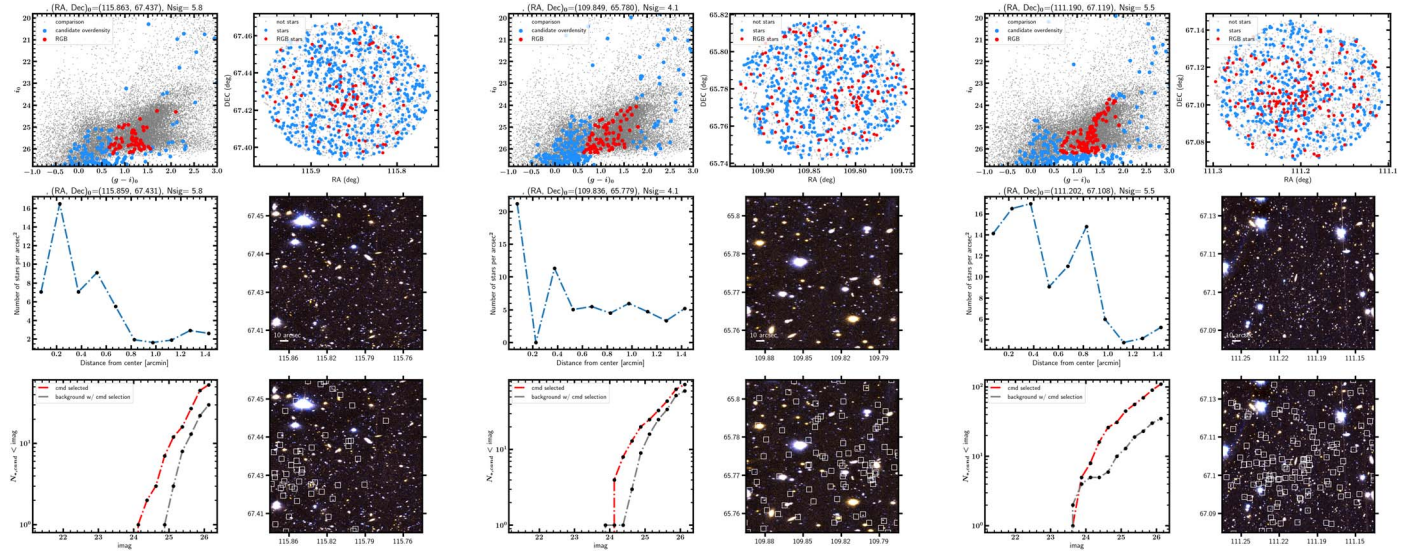

Figure 17. Diagnostic plots for the dwarfs from the top row of Figure 7, with surface brightnesses of ∼29.0 mag arcsec^{-2}, and (from left to right) $M_V \approx -6.5$, -7.5, and -8.5.

ORCID iDs

Jeffrey L. Carlin https://orcid.org/0000-0002-3936-9628
David J. Sand https://orcid.org/0000-0003-4102-380X
Burçin Mutlu-Pakdil https://orcid.org/0000-0001-9649-4815
Denija Crnojević https://orcid.org/0000-0002-1763-4128
Amandine Doliva-Dolinsky https://orcid.org/0000-0001-9775-9029
Christopher T. Garling https://orcid.org/0000-0001-9061-1697
Annika H. G. Peter https://orcid.org/0000-0002-8040-6785
Jean P. Brodie https://orcid.org/0000-0002-9658-8763
Duncan A. Forbes https://orcid.org/0000-0001-5590-5518
Jonathan R. Hargis https://orcid.org/0000-0002-8722-9806
Aaron J. Romanowsky https://orcid.org/0000-0003-2473-0369
Kristine Spekkens https://orcid.org/0000-0002-0956-7949
Jay Strader https://orcid.org/0000-0002-1468-9668
Beth Willman https://orcid.org/0000-0003-2892-9906

References

Applebaum, E., Brooks, A. M., Christensen, C. R., et al. 2021, ApJ, 906, 96
Barker, M. K., Ferguson, A. M. N., Irwin, M. J., Arimoto, N., & Jablonka, P. 2012, MNRAS, 419, 1489
Barnes, D. G., & de Blok, W. J. G. 2001, AJ, 122, 825
Battaglia, G., Taibi, S., Thomas, G. F., & Fritz, T. K. 2022, A&A, 657, A54
Bennet, P., Sand, D. J., Crnojević, D., et al. 2017, ApJ, 850, 109
Bennet, P., Sand, D. J., Crnojević, D., et al. 2019, ApJ, 885, 153
Bennet, P., Sand, D. J., Crnojević, D., et al. 2020, ApJL, 893, L9
Bosch, J., AlSayyad, Y., Armstrong, R., et al. 2019, in ASP Conf. Ser. 523, Astronomical Data Analysis Software and Systems XXVII, ed. P. J. Teuben et al. (San Francisco, CA: ASP), 521
Bosch, J., Armstrong, R., Bickerton, S., et al. 2018, PASJ, 70, S5
Brasseur, C. M., Martin, N. F., Macciò, A. V., Rix, H.-W., & Kang, X. 2011, ApJ, 743, 179
Bressan, A., Marigo, P., Girardi, L., et al. 2012, MNRAS, 427, 127
Bryan, G. L., & Norman, M. L. 1998, ApJ, 495, 80
Bullock, J. S., & Boylan-Kolchin, M. 2017, ARA&A, 55, 343
Bullock, J. S., Kravtsov, A. V., & Weinberg, D. H. 2000, ApJ, 539, 517
Carlin, J. L., Garling, C. T., Peter, A. H. G., et al. 2019, ApJ, 886, 109
Carlin, J. L., Mutlu-Pakdil, B., Crnojević, D., et al. 2021, ApJ, 909, 211
Carlin, J. L., Sand, D. J., Price, P., et al. 2016, ApJL, 828, L5
Carlsten, S. G., Greene, J. E., Beaton, R. L., Danieli, S., & Greco, J. P. 2022, ApJ, 933, 47
Cerny, W., Martínez-Vázquez, C. E., Drlica-Wagner, A., et al. 2023, ApJ, 953, 1
Chabrier, G. 2001, ApJ, 554, 1274
Chapman, S. C., Widrow, L., Collins, M. L. M., et al. 2013, MNRAS, 430, 37
Chiboucas, K., Jacobs, B. A., Tully, R. B., & Karachentsev, I. D. 2013, AJ, 146, 126
Collins, M. L. M., Karim, N., Martinez-Delgado, D., et al. 2024, MNRAS, 528, 2614
Crnojević, D., Sand, D. J., Bennet, P., et al. 2019, ApJ, 872, 80
Crnojević, D., Sand, D. J., Spekkens, K., et al. 2016, ApJ, 823, 19
Davis, A. B., Nierenberg, A. M., Peter, A. H. G., et al. 2021, MNRAS, 500, 3854
Dooley, G. A., Peter, A. H. G., Carlin, J. L., et al. 2017, MNRAS, 472, 1060
Drlica-Wagner, A., Carlin, J. L., Nidever, D. L., et al. 2021, ApJS, 256, 2
El-Badry, K., Quataert, E., Wetzel, A., et al. 2018, MNRAS, 473, 1930
Fattahi, A., Navarro, J. F., Sawala, T., et al. 2016, MNRAS, 457, 844
Forbes, D. A., Ferré-Mateu, A., Gannon, J. S., et al. 2022, MNRAS, 512, 802
Furusawa, H., Koike, M., Takata, T., et al. 2018, PASJ, 70, S3
Garling, C. T., Peter, A. H. G., Kochanek, C. S., Sand, D. J., & Crnojevic, D. 2021, MNRAS, 507, 4764
Garling, C. T., Peter, A. H. G., Spekkens, K., et al. 2024, MNRAS, 528, 365
Garrison-Kimmel, S., Bullock, J. S., Boylan-Kolchin, M., & Bardwell, E. 2017, MNRAS, 464, 3108
Gatto, A., Fraternali, F., Read, J. I., et al. 2013, MNRAS, 433, 2749
Geha, M., Mao, Y.-Y., Wechsler, R. H., et al. 2024, ApJ, 976, 118
Geha, M., Wechsler, R. H., Mao, Y.-Y., et al. 2017, ApJ, 847, 4
Griffen, B. F., Ji, A. P., Dooley, G. A., et al. 2016, ApJ, 818, 10
Hargis, J. R., Albers, S., Crnojević, D., et al. 2020, ApJ, 888, 31
Huang, S., Leauthaud, A., Murata, R., et al. 2018, PASJ, 70, S6
Hunter, J. D. 2007, CSE, 9, 90
Jahn, E. D., Sales, L. V., Wetzel, A., et al. 2022, MNRAS, 513, 2673
Jerjen, H., Rekola, R., Takalo, L., Coleman, M., & Valtonen, M. 2001, A&A, 380, 90
Jones, M. G., Mutlu-Pakdil, B., Sand, D. J., et al. 2023, ApJL, 957, L5
Ivezić, Ž., Kahn, S. M., Tyson, J. A., et al. 2019, ApJ, 873, 111
Kallivayalil, N., Sales, L. V., Zivick, P., et al. 2018, ApJ, 867, 19
Karachentsev, I. D., Makarov, D. I., & Kaisina, E. I. 2013, AJ, 145, 101
Kawanomoto, S., Uraguchi, F., Komiyama, Y., et al. 2018, PASJ, 70, 66
Komiyama, Y., Obuchi, Y., Nakaya, H., et al. 2018, PASJ, 70, S2
Mac Low, M.-M., & Ferrara, A. 1999, ApJ, 513, 142
Magnier, E. A., Schlafly, E., Finkbeiner, D., et al. 2013, ApJS, 205, 20
Mao, Y.-Y., Geha, M., Wechsler, R. H., et al. 2021, ApJ, 907, 85
Mao, Y.-Y., Geha, M., Wechsler, R. H., et al. 2024, ApJ, 976, 117
Martin, N. F., Ibata, R. A., Lewis, G. F., et al. 2016, ApJ, 833, 167
Martin, N. F., McConnachie, A. W., Irwin, M., et al. 2009, ApJ, 705, 758
Martínez-Delgado, D., Karim, N., Charles, E. J. E., et al. 2022, MNRAS, 509, 16

Martínez-Delgado, D., Romanowsky, A. J., Gabany, R. J., et al. 2012, ApJL, 748, L24
McNanna, M., Bechtol, K., Mau, S., et al. 2024, ApJ, 961, 126
McQuinn, K. B. W., Mao, Y.-Y., Buckley, M. R., et al. 2023, ApJ, 944, 14
McQuinn, K. B. W., Mao, Y.-Y., Tollerud, E. J., et al. 2024, ApJ, 967, 161
McQuinn, K. B. W., Skillman, E. D., Cannon, J. M., et al. 2010, ApJ, 721, 297
Miyazaki, S., Komiyama, Y., Kawanomoto, S., et al. 2018, PASJ, 70, S1
Moster, B. P., Somerville, R. S., Maulbetsch, C., et al. 2010, ApJ, 710, 903
Mutlu-Pakdil, B., Sand, D. J., Crnojević, D., et al. 2021, ApJ, 918, 88
Mutlu-Pakdil, B., Sand, D. J., Crnojević, D., et al. 2024, ApJ, 966, 188
Nadler, E. O., Gluscevic, V., Driskell, T., et al. 2024, ApJ, 967, 61
Ogami, I., Komiyama, Y., Chiba, M., et al. 2024, arXiv:2407.07481
Ott, J., Stilp, A. M., Warren, S. R., et al. 2012, AJ, 144, 123
Patel, E., Kallivayalil, N., Garavito-Camargo, N., et al. 2020, ApJ, 893, 121
Plummer, H. C. 1911, MNRAS, 71, 460
Price-Whelan, A. M., Sipőcz, B. M., Günther, H. M., et al. 2018, AJ, 156, 123
Rich, R. M., Collins, M. L. M., Black, C. M., et al. 2012, Natur, 482, 192
Ricotti, M., & Gnedin, N. Y. 2005, ApJ, 629, 259
Robitaille, T. P., Tollerud, E. J., Greenfield, P., et al. 2013, A&A, 558, A33
Sales, L. V., Wetzel, A., & Fattahi, A. 2022, NatAs, 6, 897
Sand, D. J., Mutlu-Pakdil, B., Jones, M. G., et al. 2022, ApJL, 935, L17
Sand, D. J., Mutlu-Pakdil, B., Jones, M. G., et al. 2024, arXiv:2409.16345
Sand, D. J., Spekkens, K., Crnojević, D., et al. 2015, ApJL, 812, L13
Santos-Santos, I. M. E., Sales, L. V., Fattahi, A., & Navarro, J. F. 2022, MNRAS, 515, 3685
Schlafly, E. F., & Finkbeiner, D. P. 2011, ApJ, 737, 103
Schlafly, E. F., Finkbeiner, D. P., Jurić, M., et al. 2012, ApJ, 756, 158
Schlegel, D. J., Finkbeiner, D. P., & Davis, M. 1998, ApJ, 500, 525
Sharina, M. E., Karachentsev, I. D., Dolphin, A. E., et al. 2008, MNRAS, 384, 1544
Simon, J. D. 2019, ARA&A, 57, 375
Simpson, C. M., Grand, R. J. J., Gómez, F. A., et al. 2018, MNRAS, 478, 548
Smercina, A., Bell, E. F., Price, P. A., et al. 2018, ApJ, 863, 152
Smercina, A., Bell, E. F., Samuel, J., & D'Souza, R. 2022, ApJ, 930, 69
Smith, S. E. T., Jensen, J., Roediger, J., et al. 2023, AJ, 166, 76
Taylor, M. 2005, in ASP Conf. Ser. 347, Astronomical Data Analysis Software and Systems XIV, ed. P. Shopbell, M. Britton, & R. Ebert (San Francisco, CA: ASP), 29
Toloba, E., Guhathakurta, P., Romanowsky, A. J., et al. 2016, ApJ, 824, 35
Tonry, J. L., Stubbs, C. W., Lykke, K. R., et al. 2012, ApJ, 750, 99
van der Walt, S., Colbert, S. C., & Varoquaux, G. 2011, CSE, 13, 22
Weisz, D. R., Dalcanton, J. J., Williams, B. F., et al. 2011, ApJ, 739, 5
Whiting, A. B., Hau, G. K. T., Irwin, M., & Verdugo, M. 2007, AJ, 133, 715
Woo, J., Courteau, S., & Dekel, A. 2008, MNRAS, 390, 1453
Zaritsky, D., Golini, G., Donnerstein, R., et al. 2024, AJ, 168, 69